WILEY | Hindawi

Research Article

Vortex-Induced Force Identification of a Long-Span Bridge Based on Field Measurement Data

S. J. Jiang,[1] Y. L. Xu [iD],[1] J. Zhu,[1] G. Q. Zhang,[1] and D. H. Dan[2]

[1]*Department of Bridge Engineering, Southwest Jiaotong University, Chengdu, China*
[2]*Department of Bridge Engineering, Tongji University, Shanghai, China*

Correspondence should be addressed to Y. L. Xu; ceylxu@swjtu.edu.cn

Vortex-induced force (VIF) identification and modelling of a long-span bridge are often conducted in terms of aeroelastic sectional model tests in wind tunnels. However, there are uncertainties inherent in wind tunnel model tests so that vortex-induced vibration (VIV) still occurs in real long-span bridges designed according to wind tunnel test results. This paper presents a framework for VIF identification of a long-span bridge based on field-measured wind and acceleration data. The framework is composed of the four steps: (1) decompose field-measured acceleration response time histories using variational mode decomposition (VMD) method; (2) obtain velocity and displacement response time histories using frequency domain integration (FDI) method; (3) establish and update the finite element model and identify the generalized VIF time histories of the bridge; and (4) identify the parameters in the polynomial VIF models and decide the most suitable VIF model. The proposed framework is finally applied to a real suspension bridge with a recent VIV event. The results show that the proposed framework can accurately identify the generalized VIF acting on the bridge from the field-measured acceleration and wind data, and the derived most suitable VIF model can produce almost the same vortex-induced response (VIR) as the measured ones.

1. Introduction

Vortex-induced vibration (VIV) of a long-span bridge is a self-excited vibration caused by the interaction of bridge motion with incoming wind. Although VIV does not directly cause a bridge to collapse, it can induce fatigue damage to crucial structural components of the bridge and impair the comfort and safety of vehicle users [1–3]. VIV has been observed on several long-span bridges worldwide, which include the Deer Isle Bridge in the USA [4], the Great Belt Bridge in Denmark [5], the Second Severn Crossing in the UK [6], the Yi Sun-Shin Bridge in Korea [7], the Xihoumen Bridge, the Yingwuzhou Bridge, and the Humen Bridge in China [2, 8, 9]. Therefore, the vortex-induced force (VIF) identification and modelling of a long-span bridge become an essential topic in order to investigate VIV and predict vortex-induced response (VIR) of a long-span bridge.

At present, VIF identification and modelling of a long-span bridge are often conducted in terms of wind tunnel

tests of aeroelastic models of bridge deck sections. The semiempirical VIF models with a few to-be decided parameters are first assumed. The vortex-induced displacement response time histories or the directly measured VIF time histories of the aeroelastic models of the bridge deck sections are then used to identify these to-be-decided parameters to yield a complete VIF model for investigating VIV and predicting VIR of the bridge.

Ehsan and Scanlan [10] regarded VIV of a bridge deck section used in the wind tunnel in the vertical direction as a single degree-of-freedom (SDOF) system and revised Scanlan's linear VIF model [11] by adding a nonlinear aeroelastic damping force to form a nonlinear VIF model. They then used the vortex-induced displacement response time histories measured from the aeroelastic model of the bridge deck section in wind tunnel to identify the parameters in the nonlinear VIF model. To improve the accuracy of parameter identification by Ehsan and Scanlan [10], Wu and Chang [12] used the identified parameter values as initial

guesses to fit both the experimental and analytical responses in the time domain. On the other hand, Barhoush et al. [13] considered VIV of a bridge deck section used in the wind tunnel in the vertical direction as a 2DOF system, in which the structural motion is modelled by a second-order linear mechanical oscillator excited by the VIF modelled by a second-order nonlinear wake oscillator (Vol del Pol type oscillator) coupled with the structural motion [14, 15]. Nevertheless, the wind tunnel test procedure used to identify the parameters in such a VIF model is complicated with considerable uncertainty [16].

The abovementioned semiempirical VIF models were established without a direct knowledge of VIF. Zhu et al. [17, 18] recently developed a new wind tunnel test technique to directly measure VIF acting on an elastically mounted deck sectional model. They also deemed VIV of the bridge deck section used in the wind tunnel in the vertical direction as a SDOF system, but they proposed the polynomial VIF models and identified the parameters in the polynomial VIF models based on the measured VIF time histories in a wind tunnel [19]. The results they obtained shed light on the characteristics of both VIF and VIV. Nevertheless, the synchronous force and vibration measurement and the data processing regarding the elimination of air-induced inertia force and damping are complex and costly.

More and more long-span bridges have now been equipped with long-term structural health monitoring systems which can measure wind and bridge responses on site [20]. Consequently, Liu et al. [21] recently identified the parameters in Scanlan's linear VIF model using on-site measurement data via the Bayesian inference-based fast Fourier transform (FFT) method. Since only the parameters in the linear VIF model were identified, the nonlinear characteristics of VIF could not be captured. Moreover, the power spectral density (PSD) of modal force due to ambient excitation and the PSD of prediction errors should be assumed in order to eliminate their effects on the VIF parameter identification. The accuracy of the Bayesian inference-based FFT method also depends significantly on the selection of frequency bandwidth. If the frequency bandwidth is not chosen appropriately, it could lead to inaccurate parameter identification.

In summary, the nonlinear VIF identification and modelling based on wind tunnel aeroelastic model test results involve many uncertainties, compared with the nonlinear VIF of a real long-span bridge. These uncertainties result from the scaling effect, blockage effect, turbulence, structural damping ratio, and Reynolds number of the wind tunnel tests. The VIF identification based on on-site measurement data currently refers to the linear VIF model only other than the nonlinear VIF of a real long-span bridge. To address the limitations of the currently used VIF identification methods, the present study aims at developing a new framework for nonlinear VIF identification and modelling of a long-span bridge using field-measured wind and acceleration data. The framework is composed of the four steps: (1) decompose field-measured acceleration response time histories using

variational mode decomposition (VMD) method; (2) obtain velocity and displacement response time histories using frequency domain integration (FDI) method; (3) establish and update the finite element model and identify the generalized VIF time histories of the bridge; and (4) identify the polynomial parameters in VIF models and decide the most suitable VIF model, as shown in Figure 1 and will be introduced in detail in the following subsections. The proposed framework will be finally applied to a real long suspension bridge with a recent VIV event to assess its feasibility and accuracy.

2. Prototype Bridge and VIV Event

2.1. Xihoumen Bridge. The Xihoumen Bridge, opened to road traffic in December 2009, is a suspension bridge crossing a narrow water way in Zhoushan, Zhejiang Province, China. The geographic location of the Xihoumen Bridge is shown in Figure 2. The Xihoumen Bridge has a main span of 1650 m and two side spans of 578 m and 485 m respectively, as shown in Figure 3(a). The north side span is supported by suspenders but the south side span of the bridge is supported by a series of piers. The bridge deck adopts a twin-box steel deck, which has a cross section of 36 m in width and 3.51 m in height. The gap between the two box girders is 6 m. The detailed geometry configuration of cross section can be found in Figure 3(b). The bridge deck carries two-way road traffic, each way having four lanes. The north and south towers of the bridge are made of reinforced concrete and have a height of 236.5 m. The main cables of the bridge are composed of parallel steel wires.

To monitor the performance and safety of the Xihoumen Bridge, a structural health monitoring (SHM) system was installed on the bridge. The SHM system has several types of sensors, including three-dimensional ultrasonic anemometers and force-balance uniaxial accelerometers [22]. Because the bridge is located in a strong wind region, monitoring wind-induced vibrations of the bridge is a major objective of the SHM system [23]. Six three-dimensional ultrasonic anemometers (denoted as UA1-UA6) were installed on the poles located at the 1/4, 1/2, and 3/4 sections of the main span at a height of 6 m above the deck surface, as shown in Figures 3 and 4. The sampling frequency of the anemometers is 20 Hz. As the anemometers are very close to the main cable in the middle of main span, only the winds recorded by the anemometers at the 1/4 and 3/4 sections of the main span can be used in this study. Three sets of force-balance uniaxial accelerometers (denoted as Acc4-Acc12) were installed at the 1/4, 1/2, and 3/4 sections of the main span and one set (denoted as Acc1-Acc3) was installed at the 1/2 section of the north side span, as shown in Figure 4. The sampling frequency of the accelerometers is 50 Hz. Each set contains three accelerometers, two installed on each side of the deck section vertically to record the vertical and torsional acceleration and one installed on the deck section horizontally to record the lateral acceleration. More detailed information on the SHM system can be found in the literature [22].
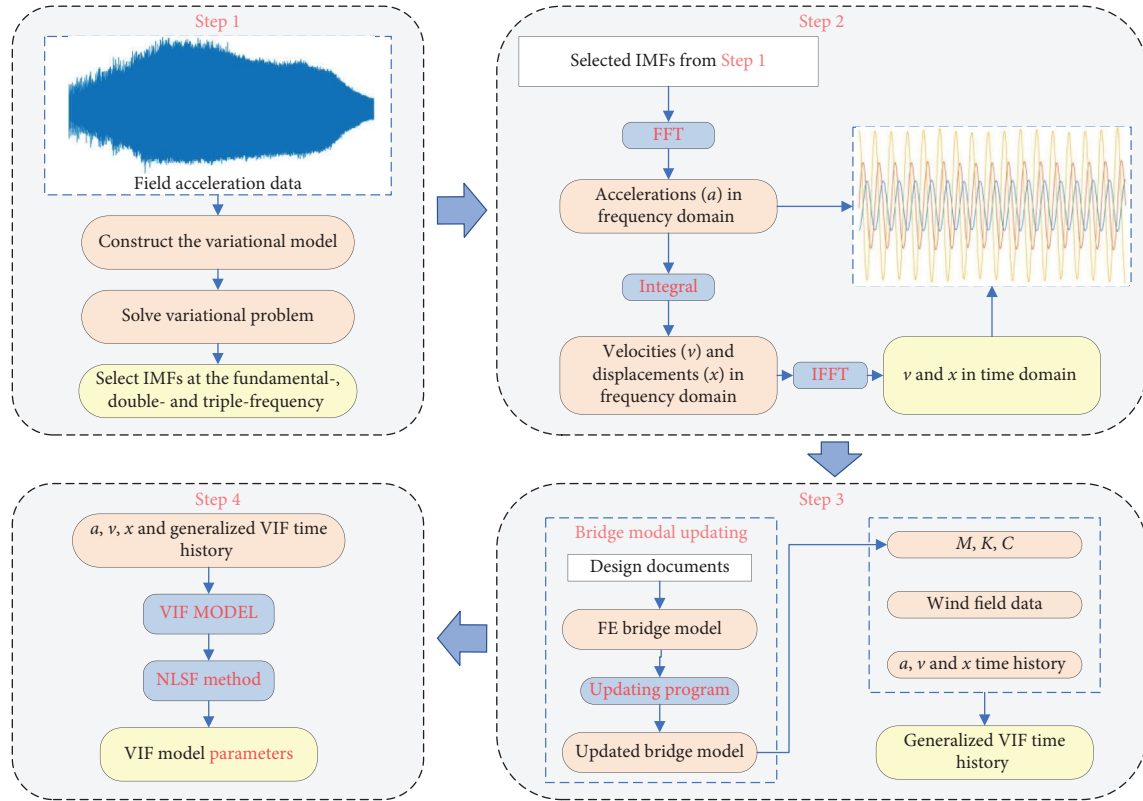
FIGURE 1: Flowchart of the proposed framework for VIF identification and modelling based on field measurement data.
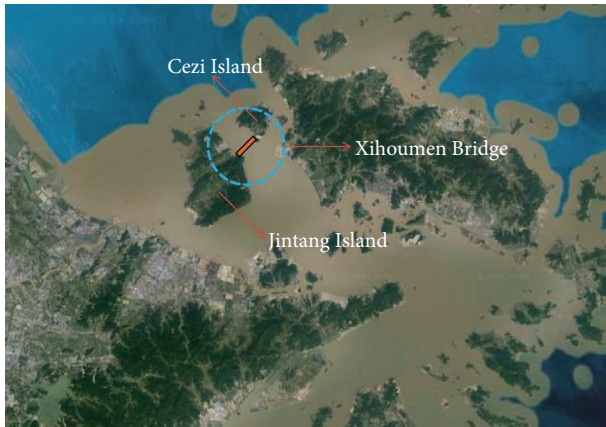

FIGURE 2: Location of Xihoumen Bridge.

2.2. FE Model of Xihoumen Bridge. The three-dimensional (3D) finite element (FE) model was established for the Xihoumen Bridge according to the bridge design drawings using the software ANSYS, as shown in Figure 5. This FE model is called the design document-based FE model. The twin-box deck was idealized as two parallel beams connected by cross beams at 3.6 m intervals. Both longitudinal and cross beams were modelled with 3D elastic beam elements with tension, compression, torsion, and bending capacities. The towers were also modelled with 3D elastic beam elements, while the main cables and suspenders were modelled with cable elements. The profile of the main cable was determined by catenary function, and the spacing distance

between two suspenders was 18 m. The main cables and towers were connected at the tower tops with coupled translational degree of freedom (DOF). The bottom of the towers and the anchorages of the main cables were modelled as fixed ends.

The design document-based FE model of the Xihoumen Bridge was used to find the modal properties of the bridge through an eigenvalue analysis. The calculated first nine vertical natural frequencies and mode shapes of the bridge are given in Table 1.

2.3. VIV Event and Field Measurement Data. On June 18, 2020, a VIV event occurred on the bridge, and the bridge was closed to traffic for the first time since it was open to the public in 2009. This VIV event lasted for a period of 66 min from 19:41 to 20:47. The anemometers and accelerometers of the SHM system timely recorded wind speed, wind direction, and the acceleration response of the bridge deck. The measurement data collected by the anemometers show that during the event, one-min mean wind speed at the deck level was 7.2 to 9.9 m/s with a wind yaw angle of approximately 143° to 150°, as shown in Figure 6. Figure 6 is a wind-rose diagram, in which the solid line represents the bridge axis, the wind direction of incoming wind is shown in the polar coordinate system, and the radius coordinate denotes the occurrence frequency of wind speeds. Since wind yaw angle is defined as the angle between the incoming wind direction and the bridge longitudinal axis, the wind yaw angle of approximately 277° to 284° indicates that the
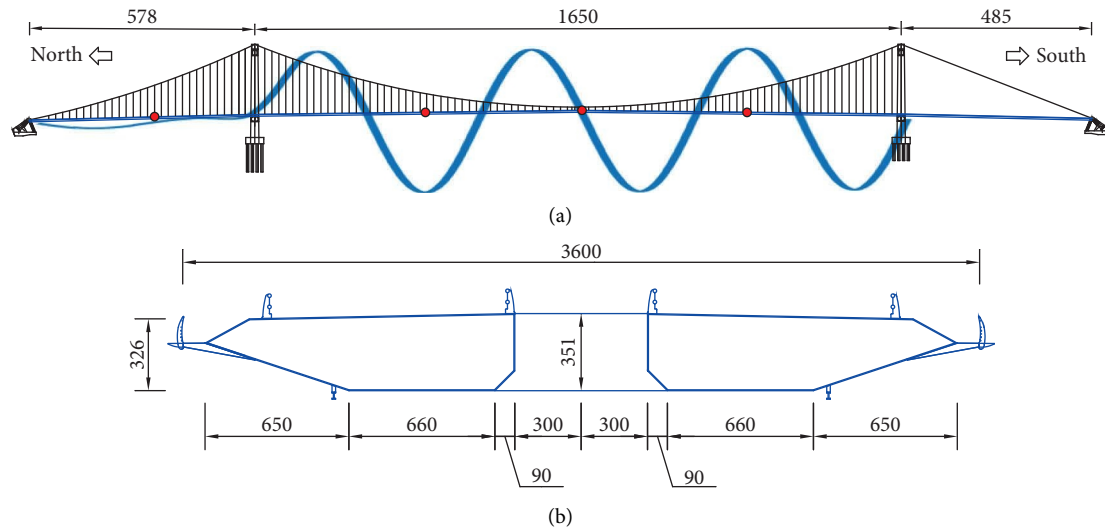
(a)

(b)

FIGURE 3: Xihoumen Bridge: (a) elevation view of the bridge (m); (b) cross section of main girder (cm).
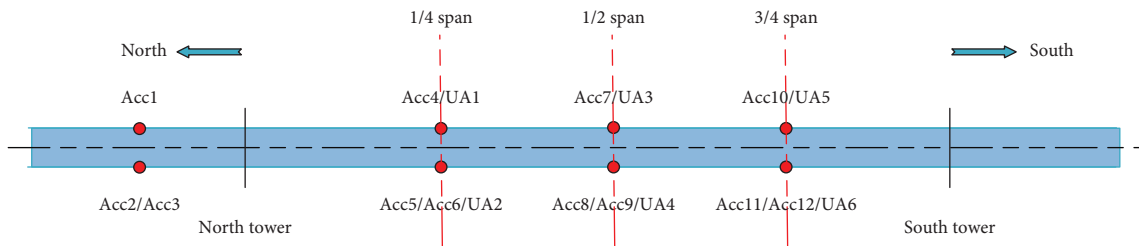

FIGURE 4: The Xihoumen Bridge and the locations of the anemometers and accelerometers.
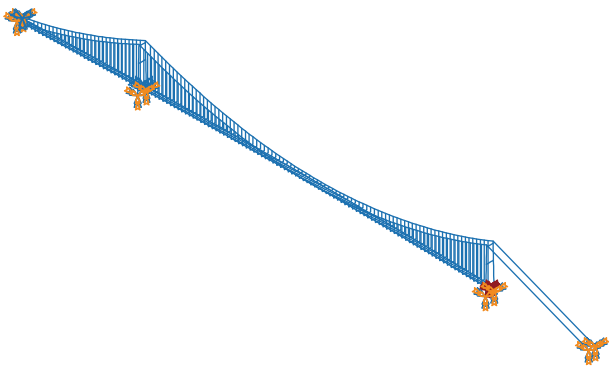

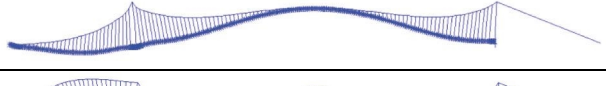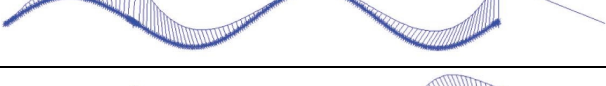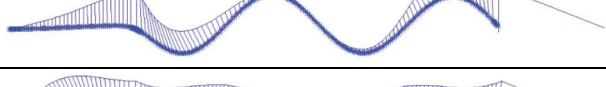FIGURE 5: Three-dimensional FE model of the Xihoumen Bridge.
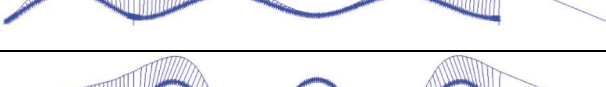
incoming wind direction was from the SE direction and almost perpendicular to the longitudinal axis of the bridge. The 10-minute turbulence intensity of the incoming wind was 5.36% to 6.2%.

The measurement data collected by the accelerometers reveals that the VIV of the bridge was dominated in the vertical direction and the dominated vibration frequency was 0.275 Hz. The 1/4 and 3/4 sections of the main span vibrated more significantly than the 1/2 section of the main span. To understand the vibration characteristics of the Xihoumen Bridge during the VIV event, Figure 7 displays

the measured vertical acceleration response of the main span at the 1/4 section and the corresponding normalized power spectral density function (PSD). It can be seen that the maximum acceleration was 0.355 m/s² at the time of 20:03. The vibration of the 1/4 section of the main span had a dominate frequency of 0.275 Hz which is close to 0.269 Hz, the 8th vertical natural frequency of the bridge calculated from the design document-based FE model of the bridge. It can be seen from Table 1 and Figure 3(a) that the 8th vertical mode shape consists of six half waves and that the 1/4 and 3/4 sections of the main span a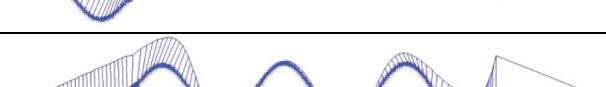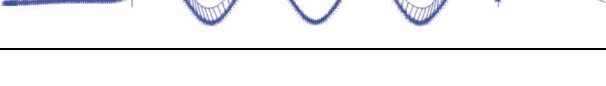re close to the maximum modal amplitude while the 1/2 section of the main span is close to the minimum modal amplitude. This is why the 1/4 and 3/4 sections of the main span vibrated more significantly than the 1/2 section of the main span during the VIV event. Therefore, it can be concluded that the VIV event of the bridge excited out the 8th vertical mode of vibration.

In consideration of the wind direction and the feature of deck vibration during the VIV event, the field wind data collected by the anemometer UA1 and the field acceleration data collected by the accelerometer Acc4 (see Figure 4) are used in subsequent analysis. Nevertheless, due to the incomplete wind data collected by the anemometer UA1, only the measurement data collected during 20:00–20:30, as shown in Figure 8, can be used for subsequent VIF identification of the bridge.

TABLE 1: The calculated first nine vertical natural frequencies and mode shapes of the bridge.

Vertical mode	Mode shapes	Natural frequencies (Hz)
1st		0.097
2nd		0.101
3th		0.133
4th		0.178
5th		0.182
6th		0.228
7th		0.260
8th		0.269
9th		0.323
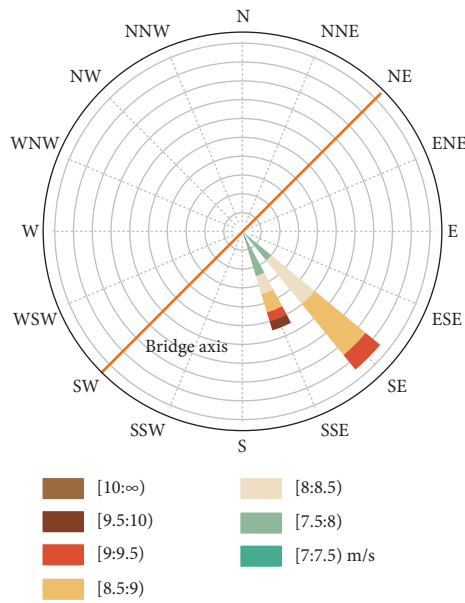
FIGURE 6: Wind-rose diagram of the bridge site.
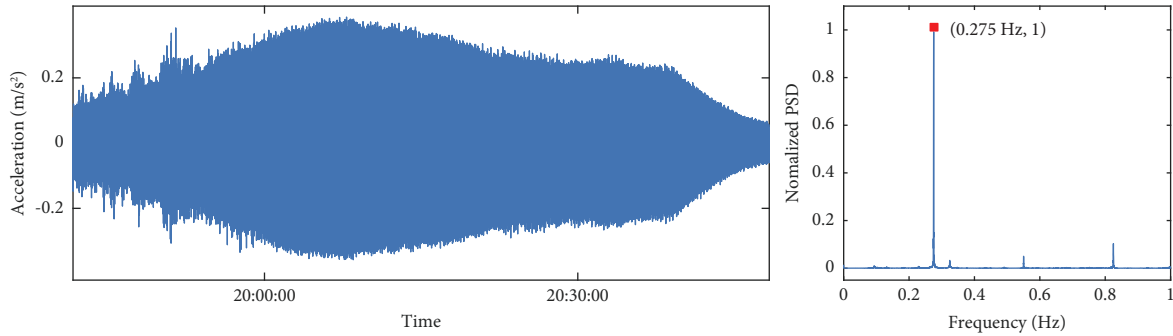
FIGURE 7: Measured vertical acceleration response time histories at the 1/4 section of the main span and the corresponding PSD during VIV event.

(a)

(b)
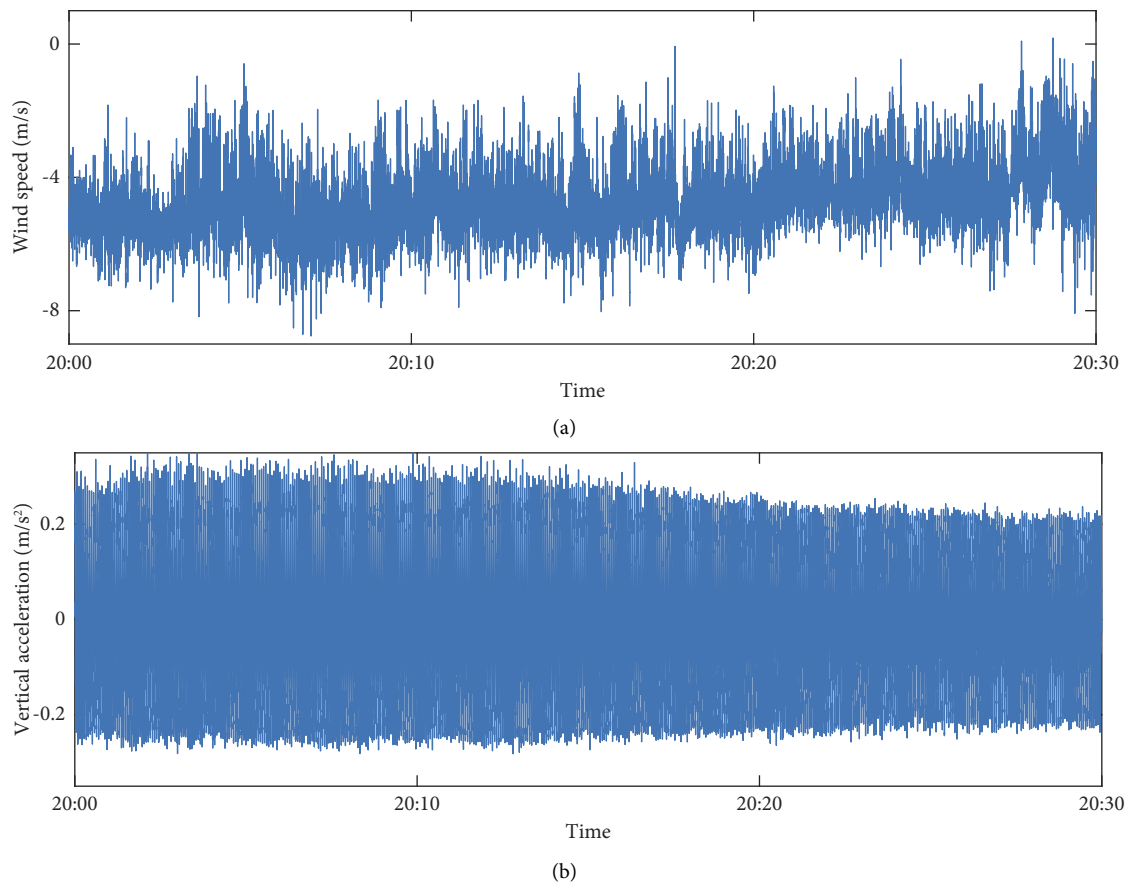
FIGURE 8: Wind speed and acceleration response time histories recorded during 20:00–20:30: (a) wind speed; (b) acceleration response.

3. Decomposition of Acceleration Data Using VMD

Although the vertical vibration of the bridge during the VIV event was mainly caused by VIF, there were still small vibration caused by buffeting force and ambient excitation. The measurement noise is also unavoidable in measurement signals. Therefore, the preprocessing of the measured acceleration time histories to eliminate their influences shall be performed to identify the VIF more accurately. Furthermore, the wind tunnel tests of VIV of the deck sectional

model showed that the VIF acting on the deck section had notable multiple-frequency components besides the component of the dominant (fundamental) frequency [18]. The PSD of the acceleration response recorded during the VIV event also shows the notable double-and triple-frequency components besides the dominant component of the 8th vertical natural frequency (see Figure 7). Therefore, an appropriate mode decomposition method shall be selected for signal processing. The variational mode decomposition (VMD) is finally selected in this study to decompose the acceleration response time histories for VIF identification.

3.1. Brief Introduction to VMD. VMD is a recently developed mode decomposition method and can be employed to decompose the original signal into a series of intrinsic mode functions (IMF) [24]. Each IMF has specific sparsity properties in the frequency domain. The central frequency and bandwidth of each function are determined by iteratively searching for the optimal solution to the variational mode. Compared with other mode decomposition methods, VMD is much more robust to sampling and noise [25, 26].

The vertical acceleration response time history, $a(t)$, collected during the VIV event is now decomposed into k IMFs. An IMF, $u_k(t)$, is considered as an amplitude-modulated-frequency-modulated signal, which can be expressed as

$$u_k(t) = A_k(t)\cos(\varphi_k(t)), \tag{1}$$

where $A_k(t)$ and $\varphi_k(t)$ represent the envelope and the phase of the kth IMF, respectively.

The above decomposition procedure can be described as a constrained variational problem with the objective function of equation (2).

$$\min_{\{u_k\},\{\omega_k\}}\left\{\sum_{k=1}^{K}\left\|\partial_t\left[\left(\delta(t)+\frac{j}{\pi t}\right)*u_k(t)\right]e^{-j\omega_k t}\right\|_2^2\right\}, \text{s.t.} \sum_{k=1}^{K}u_k(t)=a(t), \tag{2}$$

where δ is the Dirac distribution, $*$ denotes the convolution, $\{u_k\}=\{u_1,u_2,\ldots,u_k\}$ and $\{\omega_k\}=\{\omega_1,\omega_2,\ldots,\omega_k\}$ are the shorthand notations for all IMFs and their corresponding center frequencies, respectively.

Using a quadratic penalty term and Lagrangian multipliers λ, the above constrained variational problem can be transferred into an unconstrained optimization problem as

$$L(\{u_k\},\{\omega_k\},\lambda) = \alpha\sum_{k=1}^{K}\left\|\partial_t\left[\left(\delta(t)+\frac{j}{\pi t}\right)*u_k(t)\right]e^{-j\omega_k t}\right\|_2^2$$

$$+ \left\|\sum_{k=1}^{K}u_k(t)-a(t)\right\|_2^2 + \langle\lambda(t),a(t)-\sum_{k=1}^{K}u_k(t)\rangle, \tag{3}$$

where the use of quadratic penalty term is a classical approach to improve the fidelity of reconstruction. λ is commonly used to enforce constrains strictly. The combination of these two terms is used to improve the convergence properties at finite weight and the strict enforcement of the constrains [26].

In order to solve equation (3), the alternate direction method of multipliers can be used. Apply a series of iterative suboptimizations to obtain different center frequencies and the corresponding IMFs. The detailed solution process can be referred to [24].

3.2. Decompose Acceleration Response Time History. The measured vertical acceleration response at the 1/4 main span and its Fourier amplitude within 0-1 Hz during 20:00~20:30 are shown in Figures 9(a) and 9(b). Three frequencies within 0-1 Hz are clearly observed in Figure 9(b). It can be found that the energy of the measured vertical acceleration response is mainly concentrated at 0.275 Hz, 0.550 Hz, and 0.825 Hz, in which 0.550 Hz and 0.825 Hz seem to be the super harmonics of the second and third order of the fundamental exciting frequency 0.275 Hz, as observed in the wind tunnel tests [17]. The Fourier amplitude of 0.275 Hz is significantly higher than the double-frequency function (0.550 Hz) and triple-frequency function (0.825 Hz) about ten times.

The VMD is then used to decompose the measured vertical acceleration response into fundamental-frequency, double-frequency, and triple-frequency IMFs. Figures 9(c)–9(h) show the decomposed IMFs and their Fourier amplitudes. As shown in Figure 9, the independent frequency IMFs of 0.275 Hz, 0.550 Hz, and 0.825 Hz are successfully decomposed and well separated without any overlapping. Although the Fourier amplitudes of the double-frequency IMF and triple-frequency IMF are much smaller than that of the fundamental-frequency IMF in the vertical acceleration response, these two notable multiple-frequency IMFs account for a part in force time history. Moreover, these two notable multiple-frequency IMFs represent the nonlinear terms of VIV and therefore cannot be ignored.

Figure 10 is the comparison of the vertical acceleration response at 1/4 main span with and without considering multiple-frequency IMFs. It can be found that if only the fundamental-frequency IMF is considered, the vortex-induced response (VIR) will be underestimated. Therefore, considering the reasons mentioned above, these two notable multiple-frequency IMFs shall be taken in the subsequent analysis of this study. On the other hand, compared with the original measured vertical acceleration response time history shown in Figure 8, the measurement
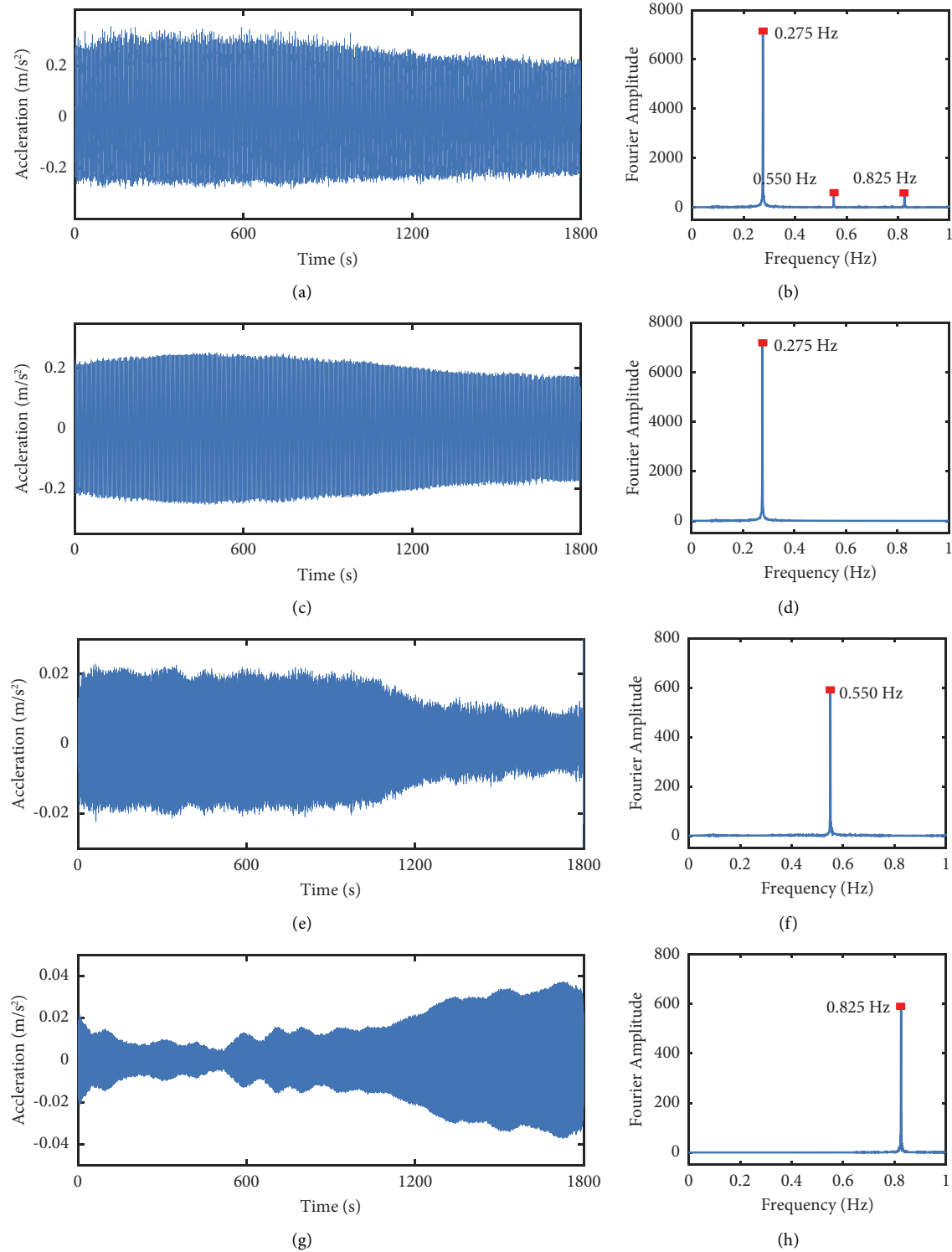
Figure 9: Measured data and decomposed intrinsic mode functions (IMFs) of vertical acceleration response at 1/4 main span and the Fourier amplitude spectrum during 20:00–20:30: (a, b) measured response; (c, d) IMF at fundamental frequency; (e, f) IMF at double-frequency; (g, h) IMF at triple-frequency.
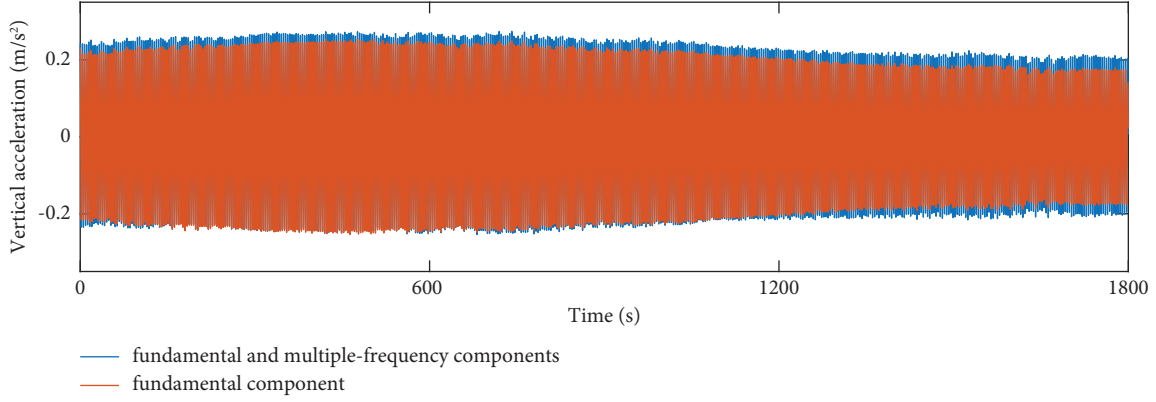
FIGURE 10: Comparison of the vertical acceleration response at 1/4 main span with and without considering multiple-frequency components.

noise of higher frequencies and the buffeting-induced responses at lower and higher frequencies are eliminated in the combination of the three IMFs.

4. Frequency Domain Integration

4.1. Theory of FDI. The frequency domain integration (FDI) method [27] uses the Fourier transform and inverse Fourier transform as well as the transfer function to reconstruct displacement and velocity response time histories from the measured acceleration response time histories. The integration is substituted by the Fourier transform, and sine and cosine transforms are directly implemented in the frequency domain so that accumulation and amplification of small errors of integration in the time domain method as well as the phase errors in the digital filter method can be avoided.

For a discrete acceleration series $a(n)$ (or IMF) with a length of N in the time domain, the Fourier transform of the series can be described by [27]

$$
\begin{cases}
a(k) = \dfrac{2}{N} \sum_{n=1}^{N} a(n) e^{[-2\pi(k-1)(n-1)i/N]} \\[2mm]
= a_k + b_k i, \\[2mm]
f(k) = \dfrac{(n-1)f_0}{2N}, \, 1 \le k \le N,
\end{cases}
\tag{4}
$$

where f_0 is the sample frequency, $a(k)$ is the complex sequence of $a(n)$ in the frequency domain after the Fourier transform, and $f(k)$ is the corresponding frequency.

Theoretically, $a(k)$ can be expressed by a simple harmonic expression as shown in equation (5), and the harmonic velocity and displacement for each frequency component can be described by equations (6) and (7).

$$
a(t)_k = A_{ak} \cos(\omega_k t + \varphi_k),
\tag{5}
$$

$$
v(t)_k = -A_{vk} \sin(\omega_k t + \varphi_k),
\tag{6}
$$

$$
x(t)_k = -A_{xk} \cos(\omega_k t + \varphi_k),
\tag{7}
$$

where $\omega_k = 2\pi f_k$ is the circular frequency of the harmonic motion; φ_k is the phase angle; $A_{ak} = \sqrt{a_k^2 + b_k^2}$, $A_{vk} = A_{ak}/\omega_k$, and $A_{xk} = A_{ak}/\omega_k^2$ are the amplitude of acceleration, velocity, and displacement harmonic motion, respectively.

It can be found from equations (5)–(7) that the phase difference is $\pi/2$ between displacement and velocity and between velocity and acceleration. The phase difference between displacement and acceleration is π. Moreover, the multiples are $2\pi f_k$ and $(2\pi f_k)^2$, respectively, between velocity and acceleration and between displacement and acceleration.

According to the principle of signal superposition, the velocity and displacement can be constructed by

$$
\begin{cases}
v(t) = \sum_{k=1}^{N} v(t)_k = -\sum_{k=1}^{N} A_{vk} \sin(\omega_k t + \varphi_k), \\[3mm]
x(t) = \sum_{k=1}^{N} x(t)_k = -\sum_{k=1}^{N} A_{xk} \cos(\omega_k t + \varphi_k).
\end{cases}
\tag{8}
$$

As a result, the frequency integration method can be explained through a Fourier transform and an inverse Fourier transform as expressed by

$$
\begin{cases}
F(v(t)) = H_v(\omega)F(a(t)) = \dfrac{1}{i\omega}F(a(t)), \\[3mm]
F(x(t)) = H_x(\omega)F(a(t)) = -\dfrac{1}{\omega^2}F(a(t)), \\[3mm]
v(t) = F^{-1}\left[\dfrac{1}{i\omega}\varphi(\omega)F(a(t))\right], \\[3mm]
x(t) = -F^{-1}\left[\dfrac{1}{\omega^2}\varphi(\omega)F(a(t))\right],
\end{cases} \tag{9}
$$

where $H_v(\omega)$ and $H_x(\omega)$ are the transfer function of $v(t)$ and $x(t)$, respectively, with respect to $a(t)$; $a(t)$ is the measured acceleration response time history; and $\varphi(\omega)$ is the accuracy function used to reduce the trend term error or drift error caused by low-frequency noise and it can be described by

$$
\varphi(\omega) = \begin{cases} 1, & 2\pi f_d \le \omega \le 2\pi f_u, \\ 0, & \text{others,} \end{cases} \tag{10}
$$

where f_d and f_u are the lower and upper of cut-off frequencies, respectively.

4.2. Obtain Velocity and Displacement Response Time Histories. The FDI method is now applied to the fundamental-frequency, double-frequency, and triple-frequency IMFs shown in Figures 9(c), 9(e), and 9(g), respectively. The lower and upper of cut-off frequency used for the fundamental-frequency, double-frequency, and triple-frequency IMFs are 0.266 Hz and 0.283 Hz, 0.543 Hz and 0.558 Hz, and 0.819 Hz and 0.831 Hz, respectively. Figure 11 shows the resulting acceleration, velocity, and displacement responses of fundamental-frequency, double-frequency, and triple-frequency IMFs in one minute. It is noted that the vertical coordinate on the left in Figure 11 is for acceleration, and velocity and displacement are plotted proportionally. It is then seen that when acceleration response is at a zero-point, the displacement response is also at the zero-point but the velocity response is at either wave peak or wave through. This satisfies the phase difference expressed by equations (5)–(7). In the fundamental-frequency IMF, the amplitudes of acceleration, velocity, and displacement responses at about 30 s are approximately 0.2166 m/s^2, 0.1251 m/s, and 0.0724 m, and the multiple is about 1.7279 ($2 \times \pi \times 0.275$). In the double-frequency IMF, the amplitudes of acceleration, velocity, and displacement responses at about 30 s are approximately 0.0175 m/s^2, 0.0051 m/s, and 0.0015 m, and the multiple is about 3.456 ($2 \times \pi \times 0.550$). In the triple-frequency IMF, the amplitudes of acceleration, velocity, and displacement responses at about 30 s are approximately 0.0162 m/s^2, 0.0031 m/s, and 0.0006 m, and the multiple is close to 5.4978 ($2 \times \pi \times 0.875$). It is seen that the three sets of IMFs all satisfy the phase difference of $\pi/2$ and the multiple

of $2\pi f_k$ as described by equations (5)–(7). Moreover, the vortex-induced displacement, velocity, and acceleration responses of the bridge at 1/4 main span can be obtained according to equation (8).

5. Model Updating and VIF Identification

To identify VIF acting on the bridge appropriately, the design document-based FE model of the bridge shall be updated by using the measurement data. This is because the 8th vertical natural frequency calculated from the design document-based FE model of the bridge is 0.269 Hz rather than 0.275 Hz. There are some uncertainties between the FE model and the prototype bridge.

5.1. Bridge Model Updating. The first step of model updating in this study is to identify the natural frequencies and modal damping ratios from the measured acceleration response time histories of the bridge at 1/4 main span. The measured acceleration response time histories of the bridge at 1/4 main span shall be ambient or buffeting-induced response time histories other than vortex-induced ones. Figure 12 shows the buffeting-induced vertical acceleration response time history of the bridge at 1/4 main span and the corresponding normalized PSD during 16:00–18:30 on June 18, 2020.

Many methods can be used to identify the modal parameters from vibration signals, such as the stochastic subspace identification [28], the power spectral method [29], the eigensystem realization algorithm [30], the fast Bayesian FFT method [31, 32], and so on. In this study, the fast Bayesian FFT method is used to identify the natural frequencies and damping ratios. This method reduces the solution of the most probable value into a four-dimensional numerical optimization problem by analyzing the mathematical structure of the posterior probability density function and solves the problem that the optimization cannot converge when the measurement freedom is large. The identified natural frequencies and damping ratios of the first six vertical modes of vibration of the bridge are listed in Table 2.

Based on the difference between the measured six vertical natural frequencies of the bridge and the corresponding ones calculated from the design document-based FE model, the objective function can be established. The parallel computing-aided FE model updating program with particle swarm optimization (PSO) algorithm is adopted for updating the mass and stiffness of the FE model of the bridge to make the difference in the selected six natural frequencies as small as possible. The selected six vertical natural frequencies from the updated FE model using the parallel computing-aided FE modal updating program mentioned above are also listed in Table 2. It is seen that the errors between the measured and calculated natural frequencies are all lower than 1%. The updated FE model of the bridge can now be used in the next section for VIF identification.
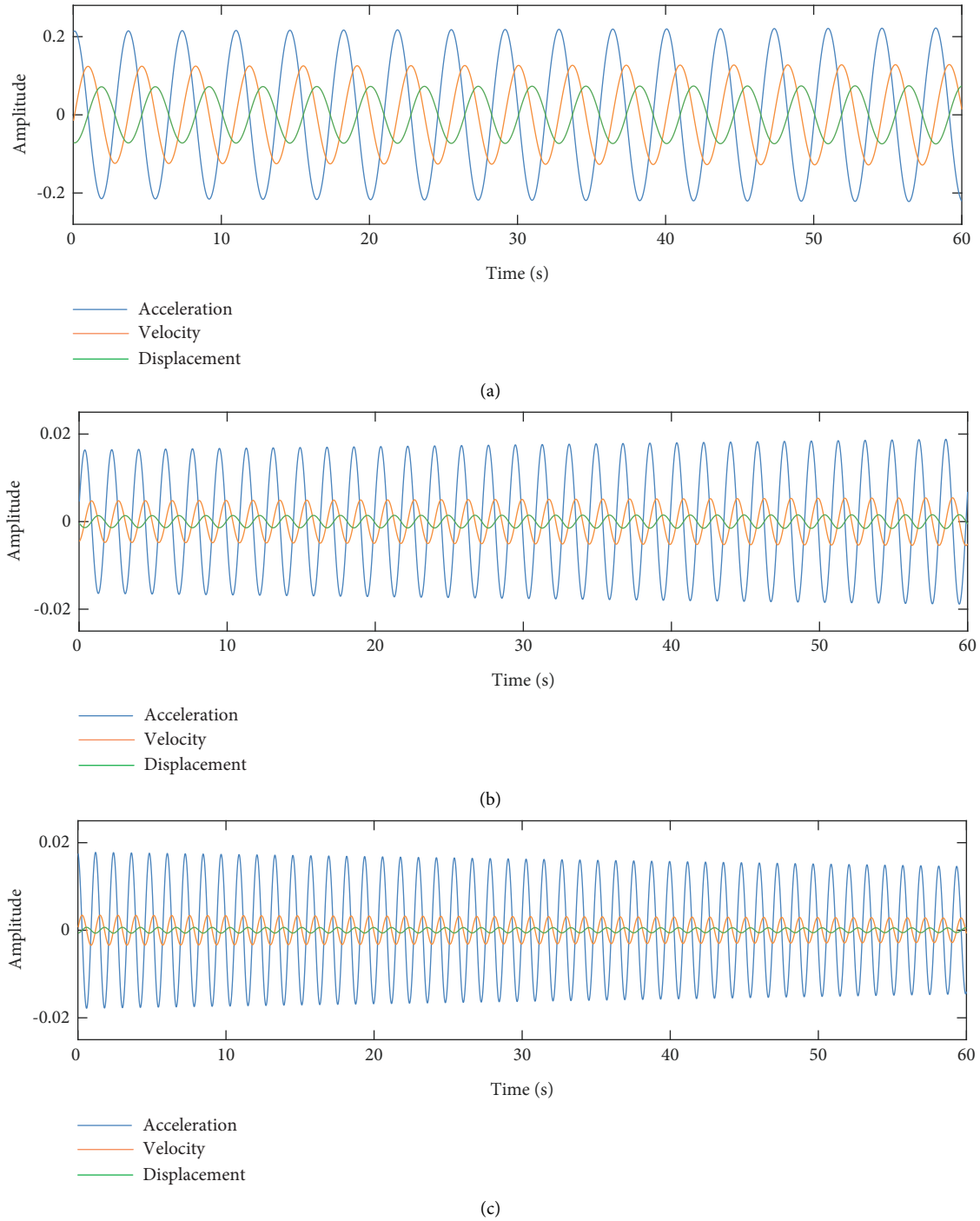
FIGURE 11: Three sets of IMFs with acceleration, velocity, and displacement in one minute at (a) 0.275 Hz, (b) 0.550 Hz, and (c) 0.825 Hz.

5.2. VIF Identification. For the sake of brevity, let us consider the bridge deck as a continuous beam. In terms of the dynamics of structures, the governing equation of motion of the bridge deck can be described by the following partial differential equation:

$$m(x)\frac{\partial^2 Z(x,t)}{\partial t^2} + c(x)\frac{\partial Z(x,t)}{\partial t} + \frac{\partial^2}{\partial x^2}\left[\text{EI}(x)\frac{\partial^2 Z(x,t)}{\partial x^2}\right] = F_{\text{VIV}}\left(Z(x,t),\frac{\partial Z(x,t)}{\partial t},x,t\right), \tag{11}$$
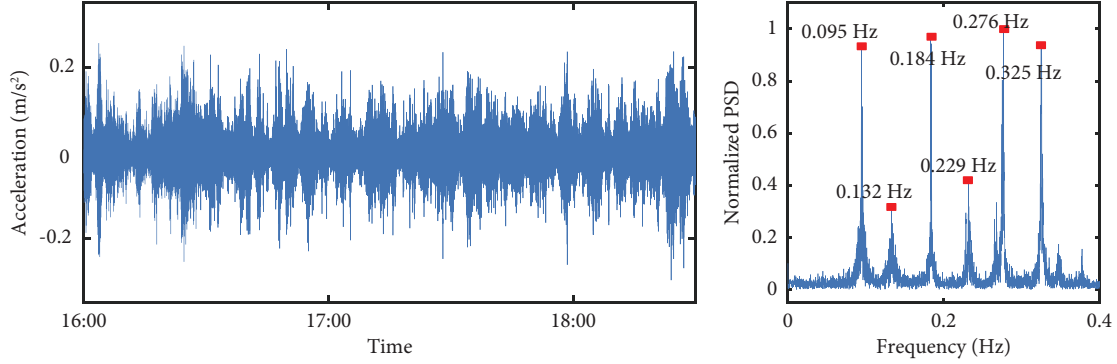
FIGURE 12: Buffeting-induced vertical acceleration response of the bridge at 1/4 main span and the corresponding PSD during 16:00–18:30.

TABLE 2: Identified modal parameters of the first six vertical modes of vibration.

Vertical mode	Identified frequency	Updated frequency	Error (%)	Identified damping ratio (%)
1st	0.0946	0.0938	0.85	0.66
3th	0.1321	0.1322	0.76	1.06
5th	0.1835	0.1828	0.38	0.18
6th	0.2290	0.2285	0.22	0.12
8th	0.2756	0.2745	0.40	0.16
9th	0.3252	0.3233	0.58	0.11

where $m(x)$, $c(x)$, and EI(x) are the mass, damping coefficient, and bending stiffness, respectively, of the bridge deck at the longitudinal coordinate x; $Z(x, t)$ is the vertical displacement of the bridge deck at the longitudinal coordinate x at time t; and $F_{\text{VIV}}(Z(x, t), (\partial Z(x, t)/\partial t), x, t)$ is the VIF acting on the bridge deck at the longitudinal coordinate x at time t and it is the function of the deck motion.

Since the vortex-induced acceleration response of the bridge deck involves the three dominant frequencies as shown in Figures 9 and 11, the three vertical modes of vibration of the bridge deck, whose natural frequencies are

most close to the corresponding dominant frequencies, should be considered. Furthermore, the vortex-induced acceleration response is obviously dominated by the 8th vertical mode of vibration at a natural frequency of 0.275 Hz, and the vortex-induced displacement response shows clearly that the concerned VIV is a weakly nonlinear vibration. Therefore, the vertical displacement response $Z(x, t)$ can be taken as the sum of the three modal responses $Z(x, t) = \sum_{i=1}^{3} y_i(x, t)$ in terms of the mode superposition method, where $y_i(x, t)$ can be expressed as $y_i(x, t) = \phi_i(x)\eta_i(t)$. As a result, equation (11) can be converted to equation (12).

$$
\int_0^L \phi_i(x)^2 m(x) \mathrm{d}x \ddot{\eta}_i(t) + \int_0^L \phi_i(x)^2 c(x) \mathrm{d}x \dot{\eta}_i(t)
$$

$$
+ \int_0^L \phi_i(x) \mathrm{EI}(x) \frac{\partial^4 \phi_i(x)}{\partial x^4} \mathrm{d}x \eta_i(t) = \int_0^L \phi_i(x) F_{\text{VIV}}^i(\eta_i(t), \dot{\eta}_i(t), x, t) \mathrm{d}x,
$$

(12)

where $\phi_i(x)$ is the concerned ith mode shape of the bridge deck; $\eta_i(t)$ is the ith generalized coordinate; and L is the length of the bridge deck.

It is worth to note that when the bridge deck undergoes VIV, VIF will induce the resonant vibration of the bridge deck at the corresponding modes of vibration, whose natural frequencies are close to the dominant frequencies of VIF.

Therefore, it is noted that the fundamental IMF at 0.275 Hz (see Figure 9) corresponds to the mode of vibration at 0.275 Hz, the double-frequency IMF at 0.550 Hz corresponds to the mode of vibration at 0.549 Hz, and the triple-frequency IMF at 0.825 Hz corresponds to the mode of vibration of 0.824 Hz.

Introduce the generalized mass M_i, damping C_i, stiffness K_i, and VIF $\widehat{f}_{\text{VIV}}^i$ as follows:

$$
\begin{cases}
M_i = \displaystyle\int_0^L \phi_i(x)^2 m(x)\mathrm{d}x, \\[4mm]
C_i = \displaystyle\int_0^L \phi_i(x)^2 c(x)\mathrm{d}x, \\[4mm]
K_i = \displaystyle\int_0^L \phi_i(x)\mathrm{EI}(x)\frac{\partial^4 \phi_i(x)}{\partial^4 x}\mathrm{d}x, \\[4mm]
\widehat{f}^{\,i}_{\mathrm{VIV}} = \displaystyle\int_0^L \phi_i(x)F^i_{\mathrm{VIV}}\left(\eta_i(t),\dot{\eta}_i(t),x,t\right)\mathrm{d}x.
\end{cases}
\tag{13}
$$

By considering the section of the bridge deck at 1/4 main span with the mode shape value of ϕ_i (1/4 main span), $\eta_i(t)$ can be obtained by y_i (1/4 main span, t)/ϕ_i (1/4 main span). Then, calculate $\dot{\eta}_i(t)$ and $\ddot{\eta}_i(t)$ in the same way. The governing equation of motion of the bridge deck under vertical VIF, equation (12), can be rewritten as equation (14).

$$
M_i \ddot{y}_i\!\left(\frac{1}{4}\text{ main span}, t\right) + C_i \dot{y}_i\!\left(\frac{1}{4}\text{ main span}, t\right) + K_i y_i\!\left(\frac{1}{4}\text{ main span}, t\right)
$$
$$
= \phi_i\!\left(\frac{1}{4}\text{ main span}\right)\widehat{f}^{\,i}_{\mathrm{VIV}}\left(y_i(t),\dot{y}_i(t),t\right),
\tag{14}
$$

where M_i is the ith generalized mass; $C_i = 2\zeta_i\omega_i M_i$ is the ith generalized damping; ζ_i is the ith damping ratio; ω_i is the ith circular frequency of the bridge deck, which can be obtained from the updated bridge model; $K_i = \omega_i^2 M_i$ is the ith generalized stiffness; and $\widehat{f}^{\,i}_{\mathrm{VIV}}$ is the ith generalized VIF.

The generalized VIF time histories for the three modes of vibration of the bridge deck during the VIV event can be identified using equation (14). It is worth noting that the VIF, when the bridge deck undergoes VIV, is small compared with the inertia force or the restoring force of the bridge deck. To ensure the accuracy of the identified VIF, the generalized VIF is calculated by the sum of the generalized inertia force, restoring force, and damping force. This is because the VIV can be approximately seen as a simple harmonic motion in the given mode of vibration and the sum of the generalized inertial and restoring force is small compared with the generalized damping force. Furthermore, to escalate the identification accuracy of the generalized VIF, the generalized modal properties calculated from the updated finite element model of the bridge obtained in Section 5.1, the model damping ratios identified from the field-measured acceleration time histories and given in Section 5.1, the acceleration time histories obtained by decomposing the field-measured acceleration time histories through VMD in Section 3, the velocity and displacement time histories obtained by FDI in Section 4 are used in the identification of the generalized VIF in equation (14).

To have a good understanding of VIV and VIF of the concerned bridge deck, the half-hour measurement data are divided into 30 sets of one-minute data in the subsequent VIF identification. Figures 13(a)–13(c) show the identified generalized VIF time histories in one minute for the three modes of vibration, respectively. It is seen that the identified generalized VIF at the fundamental frequency is in the range of −12.24 to 12.24 N, the identified generalized VIF at the

double-frequency is in the range of −1.88 to 1.88 N, and the identified generalized VIF at the triple-frequency is in the range of −4.81 to 4.81 N. It is noted that the mode shapes are normalized with respect to the mass matrix and the generalized VIFs are calculated with respect to the normalized mode shapes in this study. Furthermore, the generalized VIFs are used only for the subsequent VIF parametric identification and there is no attempt to identify the VIF of the bridge deck directly. The identified generalized VIFs are also called the measured generalized VIFs in the next section for the sake of brevity.

6. VIF Parametric Identification

6.1. VIF Model for Twin-Box Decks under Turbulent Wind. During the last decades, several semiempirical VIF models have been proposed, based on the wind tunnel test results of elastically mounted section models, to predict the VIR of the prototype bridge [10, 17, 33]. The Scanlan-nonlinear VIF model [10] is most widely used in predicting the VIR of the bridge because it only requires a single wind tunnel test to identify the main parameters in the VIF model. Nevertheless, Zhu et al. [17] found that the Scanlan-nonlinear model could predict the maximum amplitude of VIR with satisfaction but it could not give the time history of the measured VIF satisfactorily. Zhu et al. [17] then proposed a new semiempirical VIF model for a single-box deck section, as shown in (15), in which the cubic term $(\eta/D)^2 \dot{\eta}/U$ in the Scanlan-nonlinear model was replaced by $(\dot{\eta}/U)^3$. Compared with the Scanlan-nonlinear model, this model could predict both the VIR and VIF well.

$$
\widetilde{f}_{\mathrm{VIV}} = \frac{1}{2}\rho U^2 D\left[Y_1\left(1 - \varepsilon_1\left(\frac{\dot{\eta}}{U}\right)^2\right)\frac{\dot{\eta}}{U} + Y_2\frac{\eta}{D}\right],
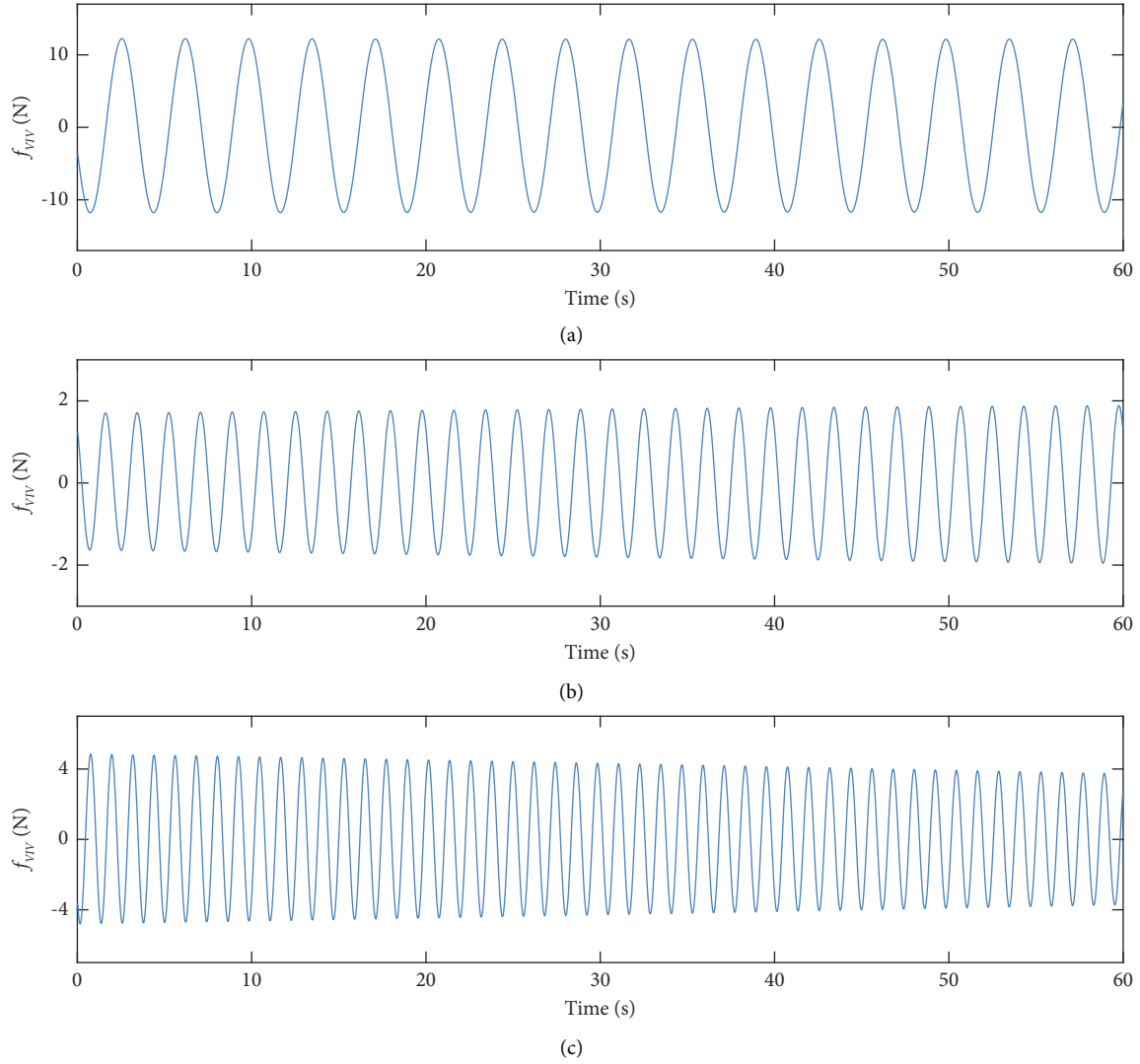\tag{15}
$$

Figure 13: Identified VIF time histories for the three modes of vibration in one minute at (a) 0.275 Hz, (b) 0.550 Hz, and (c) 0.825 Hz.

where ρ is the air density, U is the mean wind speed, D is the characteristic length of the bridge, and Y_1, Y_2, and ε_1 are the coefficients of self-excited force (VIF).

The VIF model expressed by equation (15) was established based on the wind tunnel test, in which VIV of a bridge deck section is regarded as a SDOF system. From the amplitude spectrum of the measured VIF by Zhu et al. [17], one can find that besides the significant amplitude of VIF at the fundamental frequency, the amplitudes of VIF at the multiple frequencies also occupy considerable proportion. However, owing to the bridge deck section in the wind tunnel test being a SDOF system, the VIF at the

multiple frequencies could not induce the resonant vibration of the corresponding modes of vibration, except for the VIF at the fundamental frequency. Nevertheless, when VIV occurs in a real bridge, the bridge is a multi-degree-of-freedom system and the multiple-frequency VIF can induce the resonant vibration of the corresponding modes of vibration. Therefore, the VIF model proposed by Zhu et al. [17] for the SDOF system is not applicable in this study. To describe the VIF more accurately, a general polynomial VIF model for a twin-box deck with all the linear terms, quadratic nonlinear terms, and cubic nonlinear terms is adopted in this study.

$$\widetilde{F}_{\text{VIV}}^{i} = \frac{1}{2}\rho U^2 D\left[Y_1\frac{\dot{\eta}_i}{U} + Y_2\frac{\eta_i}{D} + Y_3\left(\frac{\dot{\eta}_i}{U}\right)^2 + Y_4\frac{\dot{\eta}_i}{U}\frac{\eta_i}{D} + Y_5\left(\frac{\eta_i}{D}\right)^2\right.$$

$$\left. - Y_1\varepsilon_1\left(\frac{\dot{\eta}_i}{U}\right)^3 - Y_1\varepsilon_2\left(\frac{\dot{\eta}_i}{U}\right)^2\frac{\eta_i}{D} - Y_1\varepsilon_3\frac{\dot{\eta}_i}{U}\left(\frac{\eta_i}{D}\right)^2 - Y_1\varepsilon_4\left(\frac{\eta_i}{D}\right)^3\right], \tag{16}$$

$$\widetilde{f}_{\text{VIV}}^{i} = \int_0^L \widetilde{F}_{\text{VIV}}^{i}\phi_i(x)\mathrm{d}x,$$

where $Y_1, Y_2, Y_3, Y_4, Y_5, \varepsilon_1, \varepsilon_2, \varepsilon_3, \varepsilon_4$ are the nine to-be-determined parameters in the VIF model and $\widetilde{f}_{\text{VIV}}^{i}$ is the ith generalized VIF to be computed.

$$R\left(Y_1, Y_2, Y_3, Y_4, Y_5, \varepsilon_1, \varepsilon_2, \varepsilon_3, \varepsilon_4\right) = \sum_{i=1}^{3}\left(\sum_{j=1}^{n}\left(\widetilde{f}_{\text{VIV}}^{i}(t_j) - \widehat{f}_{\text{VIV}}^{i}(t_j)\right)^2\right), \tag{17}$$

where $\widehat{f}_{\text{VIV}}^{i}(t_j)$ and $\widetilde{f}_{\text{VIV}}^{i}(t_j)$ are the values of the generalized VIFs at time t_j, determined according to equations (14) and (16), respectively, and n is the total number of the data point in one minute.

The parameters $Y_1, Y_2, Y_3, Y_4, Y_5, \varepsilon_1, \varepsilon_2, \varepsilon_3$, and ε_4 can be identified by seeking the minimal value of the target residue function expressed by equation (17). The Levenberg–Marquardt method is used for optimization [33]. Since one-minute time history is used for identification, 30 groups of VIF parameters can be obtained. Afterwards, equation (16) can be used to calculate the VIF. Figures 14(a)–14(d) shows the scatters between the computed and measured amplitudes of acceleration responses and three generalized VIFs at each time step of 0.02 s during 20:00–20:30. The solid line is the straight line with the slope of 1. If the scatters are closer to the solid line, the identified VIF parameters are of high accuracy for the concerned quantity. It can be found from Figure 14(a) that the scatters of acceleration response amplitude are so close to the solid line that the identified VIF parameters are of high accuracy for the acceleration responses. It is clear to see from Figures 14(b)–14(d) that the discreteness of the first and third generalized VIFs is relatively larger and the discreteness of the second generalized VIF is the largest, compared with the acceleration response. One of the reasons could be because the value of the double-frequency VIF is smaller than that of the fundamental-frequency and triple-frequency VIF. Nevertheless, the identified VIF parameters still process enough accuracy for the three generalized VIFs.

6.3. Validation of Obtained VIF Model.
To validate the identified VIF parameters in the VIF model, Figures 15(a)–15(h) present the comparative results of time histories and Fourier amplitude spectra between the computed and measured acceleration responses and the three generalized

6.2. Parametric Identification via NLSF.
The parameters in the VIF model expressed by equation (16) can be identified based on the measured generalized VIF time histories in Section 5 through the nonlinear least squares fitting (NLSF). The target residue function in NLSF is defined as follows:

VIFs in one minute. Figures 15(a) and 15(b) show the comparison between the computed and measured acceleration response time histories and Fourier amplitude spectra for a wind speed of $U = 8.8$ m/s in one minute. It can be seen that the computed acceleration time history agrees well with the measured one in general. One can also find that the computed Fourier amplitude spectrum also agrees well with the measured one at the three dominant frequencies. Figures 15(c)–15(h) display the comparisons between the computed and measured first, second, and third generalized VIF time histories and Fourier amplitude spectra for a wind speed of $U = 8.8$ m/s in one minute. The computed first and third generalized VIF time histories and Fourier amplitude spectra agree well with the measured ones, except for only small errors in the fitting of high peaks. Nevertheless, Figures 15(e) and 15(f) show that there are some differences between the computed and measured second generalized VIF time histories and Fourier amplitude spectra.

6.4. Further Analysis of Parameters in VIF Model.
There are a total of nine parameters, associated with the nine terms, in the VIF model expressed by equation (16). It is of practical interest to know whether some parameters and some terms in the VIF model can be dropped without significant influence on the accuracy of the VIF model. A self-adaptive simplification method (SASM) is thus proposed to determine the importance of each parameter/term in the VIF model for the Xihoumen Bridge and find the most suitable VIF model. R-squared (R) is a common measure that provides information about the goodness of fit of a model by taking a value within the range from 0 to 1. When R equals 1, the model fits the data perfectly and when R equals 0, the model fails to explain the data. In this study, R_i between the measured i^{th} generalized VIF $\widehat{f}_{\text{VIV}}^{i}$ and the computed i^{th} generalized VIF $\widetilde{f}_{\text{VIV}}^{i}$ is defined as

(a)   (b)   (c)   (d)
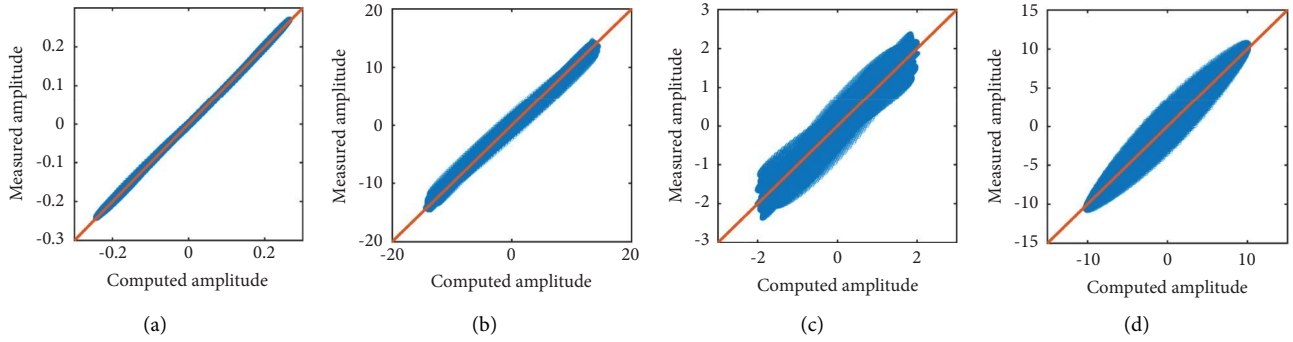
FIGURE 14: Scatters between computed and measured amplitudes: (a) acceleration response; (b) the first generalized VIF; (c) the second generalized VIF; (d) the third generalized VIF.
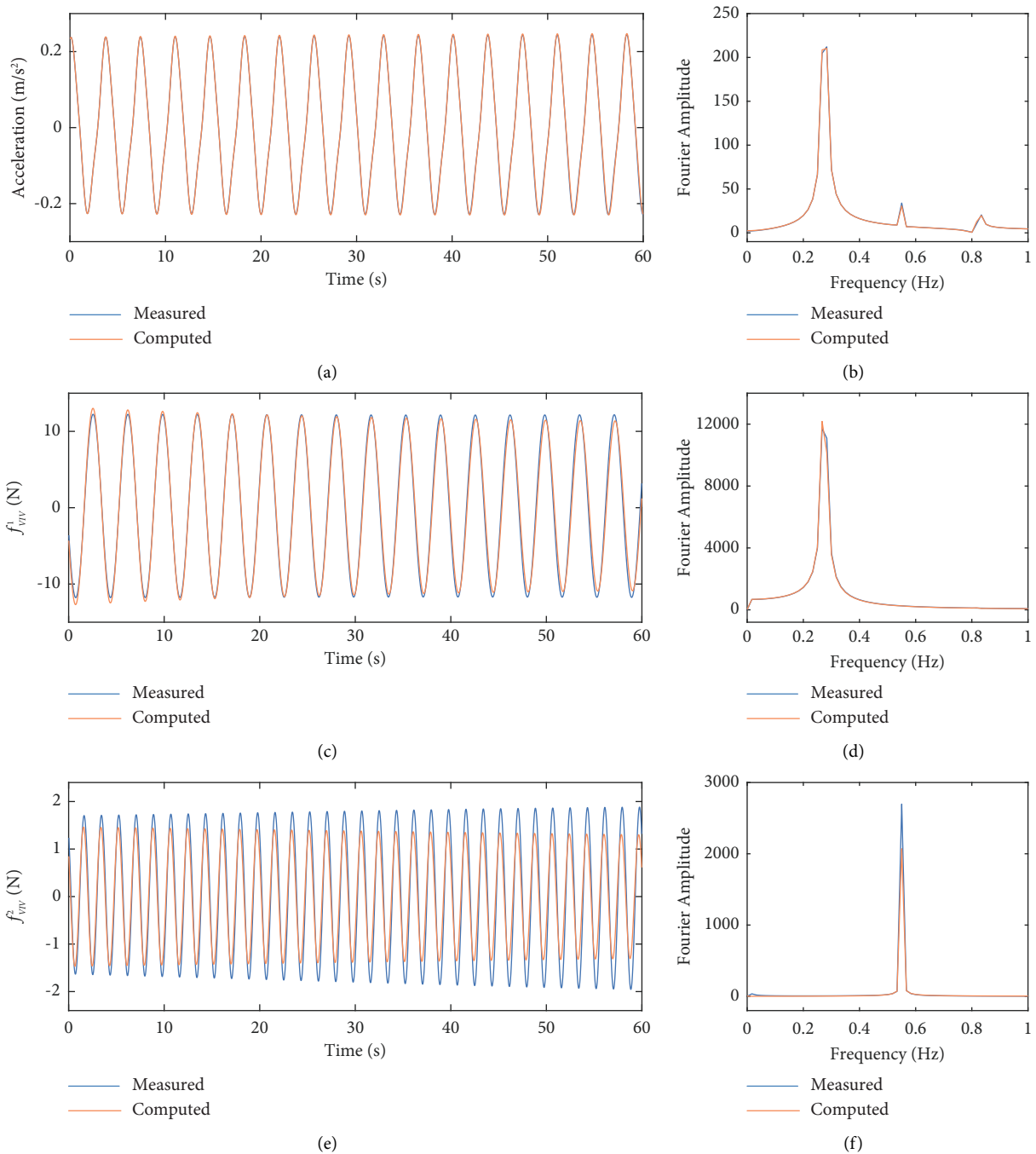

(a)

(b)

(c)

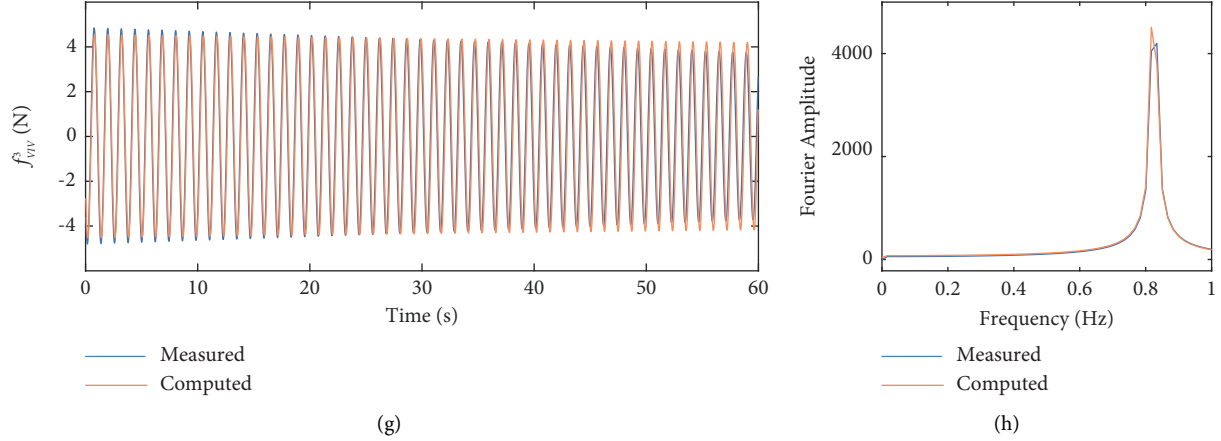(d)

(e)

(f)

FIGURE 15: Continued.

(g)

(h)

FIGURE 15: Comparisons of time histories and amplitude spectra between the computed and measured acceleration responses and three generalized VIFs: (a, b) acceleration response; (c, d) the first generalized VIF; (e, f) the second generalized VIF; (g, h) the third generalized VIF.

$$R_i = \frac{1}{30} \sum_{k=1}^{30} \left(1 - \frac{SSE_k^i}{SST_k^i} \right), \tag{18}$$

$$SSE_k^i = \sum_{j=1}^{n} \left[\tilde{f}_{VIV}^i(t_j)_k - \hat{f}_{VIV}^i(t_j)_k \right]^2, \tag{19}$$

$$SST_k^i = \sum_{j=1}^{n} \left[\hat{f}_{VIV}^i(t_j)_k - \overline{f}_{VIV\_k}^i \right]^2, \tag{20}$$

where n is the number of data points in one-minute; k is the number of one-minute samples; SSE is the sum squared error between the measured i^{th} generalized VIF $\hat{f}i_{VIV}^i$ and the computed i^{th} generalized VIF $\tilde{f}_{VIV}^i$, obtained by equations (14), (16), and (19) in order; and SST is the sum squared error between the measured i^{th} generalized VIF $\hat{f}_{VIV}^i$ and the average measured i^{th} generalized VIF $\overline{f}_{VIV}^i$, calculated by equations (14) and (20) in order.

Table 3 lists the R_1, R_2, R_3 values and the corresponding parameters involved in the VIF model. It is seen that when all the linear terms, quadratic nonlinear terms, and cubic nonlinear terms in the VIF model expressed by equation (16) are taken (1st line in Table 3), the first generalized VIF time history has a high degree of fit and the value of R_1 is 0.99. The second and third generalized VIF time histories also have an acceptable degree of fit and the values of R_2 and R_3 are 0.86 and 0.89, respectively. The importance of each parameter in the VIF model expressed by equation (16) is tested by eliminating the associated term one by one. The results shown in Table 3 finally confirm that if the parameters Y_3, Y_4 and Y_5 are eliminated, the values of $R_1, R_2,$ and R_3 are still 0.99, 0.84, and 0.89, respectively (12th line in Table 3). Since these R values are almost the same as those with all the terms included in the VIF model, one may conclude that all the quadratic nonlinear terms in equation (16) can be taken away without influence on the accuracy of the VIF model. This VIF model is called the simplified VIF model.

TABLE 3: Analysis of the parameters in the VIF model.

Parameters in the model	R_1	R_2	R_3	Accepted
$Y_1, Y_2, Y_3, Y_4, Y_5, \varepsilon_1, \varepsilon_2, \varepsilon_3, \varepsilon_4$	0.99	0.86	0.89	Yes
$Y_2, Y_3, Y_4, Y_5, \varepsilon_1, \varepsilon_2, \varepsilon_3, \varepsilon_4$	0.22	0.04	0.07	No
$Y_1, Y_3, Y_4, Y_5, \varepsilon_1, \varepsilon_2, \varepsilon_3, \varepsilon_4$	0.99	0.36	0.27	No
$Y_1, Y_2, Y_4, Y_5, \varepsilon_1, \varepsilon_2, \varepsilon_3, \varepsilon_4$	0.99	0.82	0.89	Yes
$Y_1, Y_2, Y_3, Y_5, \varepsilon_1, \varepsilon_2, \varepsilon_3, \varepsilon_4$	0.99	0.83	0.89	Yes
$Y_1, Y_2, Y_3, Y_4, \varepsilon_1, \varepsilon_2, \varepsilon_3, \varepsilon_4$	0.99	0.82	0.89	Yes
$Y_1, Y_2, Y_3, Y_4, Y_5, \varepsilon_2, \varepsilon_3, \varepsilon_4$	0.86	0.59	0.58	No
$Y_1, Y_2, Y_3, Y_4, Y_5, \varepsilon_1, \varepsilon_3, \varepsilon_4$	0.99	0.22	0.48	No
$Y_1, Y_2, Y_3, Y_4, Y_5, \varepsilon_1, \varepsilon_2, \varepsilon_4$	0.93	0.68	0.67	No
$Y_1, Y_2, Y_3, Y_4, Y_5, \varepsilon_1, \varepsilon_2, \varepsilon_3$	0.99	0.11	0.44	No
$Y_1, Y_2, Y_5, \varepsilon_1, \varepsilon_2, \varepsilon_3, \varepsilon_4$	0.99	0.85	0.89	Yes
$Y_1, Y_2, \varepsilon_1, \varepsilon_2, \varepsilon_3, \varepsilon_4$	0.99	0.84	0.89	Yes
$Y_1, Y_2, \varepsilon_1, \varepsilon_2, \varepsilon_4$	0.93	0.68	0.67	No
$Y_1, Y_2, \varepsilon_2, \varepsilon_3, \varepsilon_4$	0.86	0.59	0.58	No
$Y_1, \varepsilon_1, \varepsilon_2, \varepsilon_3, \varepsilon_4$	0.99	0.36	0.27	No
$Y_1, Y_2, \varepsilon_1, \varepsilon_3, \varepsilon_4$	0.99	0.21	0.48	No
$Y_1, Y_2, \varepsilon_1, \varepsilon_2, \varepsilon_3$	0.99	0.10	0.44	No
$Y_2, \varepsilon_1, \varepsilon_2, \varepsilon_3, \varepsilon_4$	0.22	0.04	0.07	No

Figures 16(a)–16(d) shows the scatters between the computed amplitudes by the simplified VIF model and the measured amplitudes of acceleration responses and three generalized VIFs at each time step of 0.02 s during 20:00–20:30. It is seen that the simplified VIF model has a high accuracy to describe acceleration responses and VIF time histories. The relationships between the identified parameters in the simplified VIF model and the mean wind speed are also explored based on field-measured acceleration data and wind data via the procedure shown in Figure 1. The variations of identified parameters in the simplified VIF model with mean wind speed are shown in Figure 17. The black circular points represent the correlation between the mean wind speed and VIF parameters. It is seen from Figure 17 that there is a linear correlation between each VIF parameter and mean wind speed.
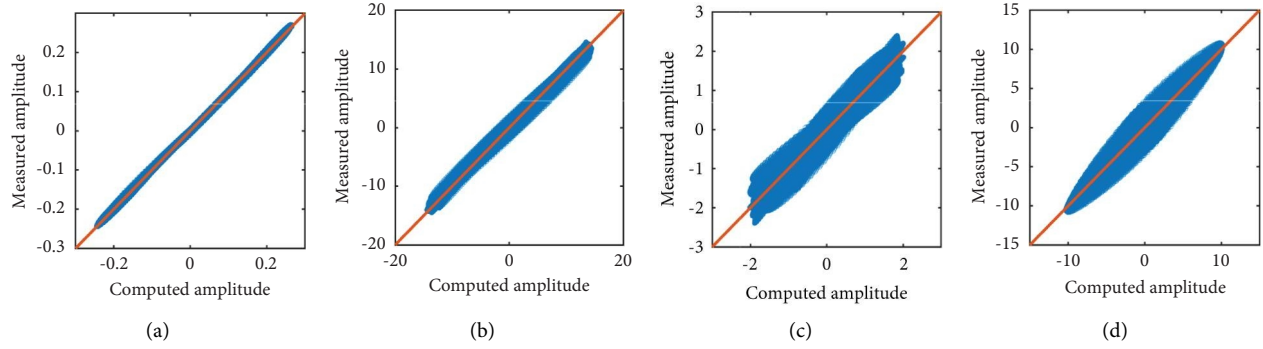
FIGURE 16: Scatters between the computed amplitudes by the simplified VIF model and the measured amplitudes: (a) acceleration response; (b) the first generalized VIF; (c) the second generalized VIF; (d) the third generalized VIF.
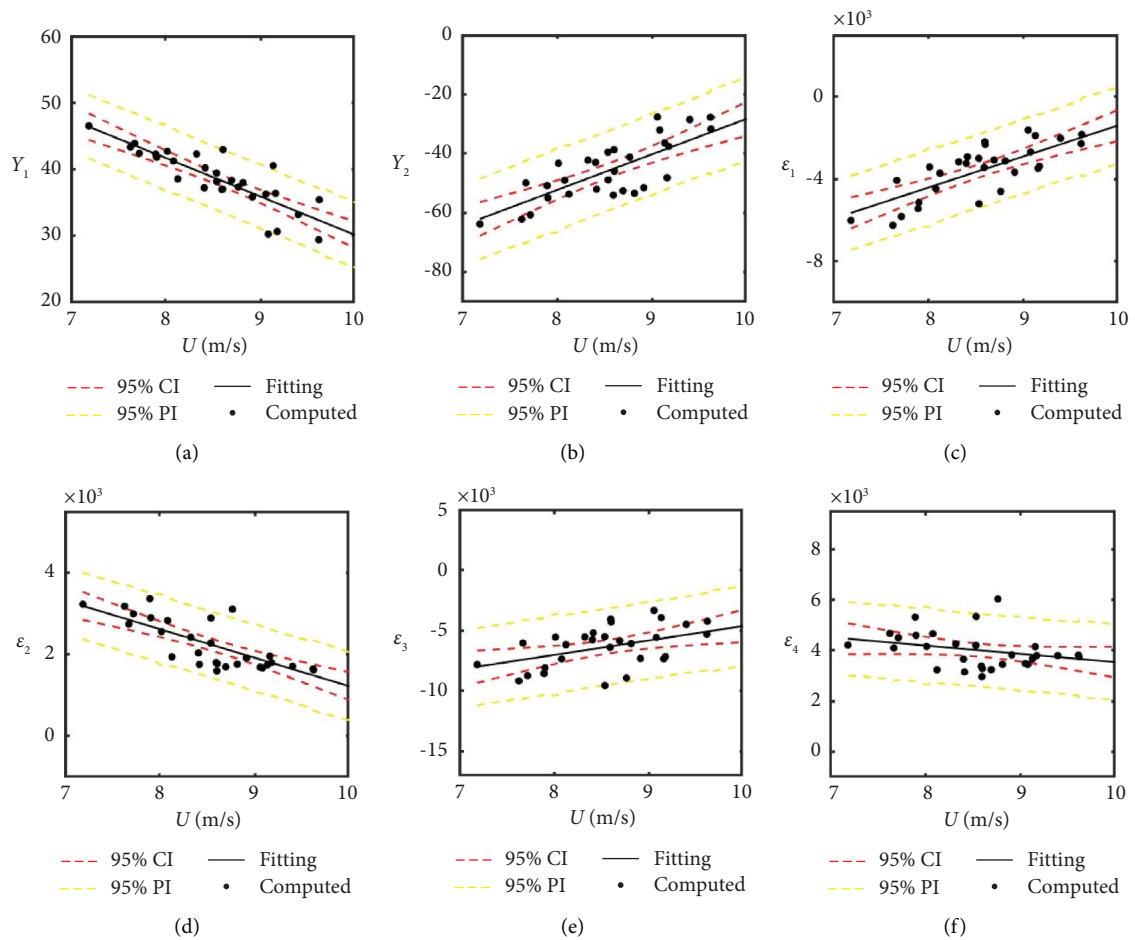

FIGURE 17: Variations of identified parameters in the simplified VIF model with mean wind speed: (a) Y_1; (b) Y_2; (c) ε_1; (d) ε_2; (e) ε_1; (f) ε_2.

7. Concluding Remarks

The framework for VIF identification of a long-span bridge based on field-measured wind and acceleration data has been proposed in this study. The proposed framework has been applied to a real suspension bridge with a recent VIV event. The major findings and conclusions from this study can be summarized as follows:

(1) By analyzing the measured acceleration data of the real suspension bridge during the VIV event, it is found that the vortex-induced acceleration responses are dominated by three frequencies: fundamental frequency of 0.275 Hz, double-frequency of 0.550 Hz, and triple-frequency of 0.825 Hz. These three dominant frequencies correspond to the 8th, 14th, and 23th modes of vibration of the bridge.

(2) By using the variational mode decomposition (VMD), the three intrinsic mode functions (IMFs) are successfully extracted from the measured acceleration response time history. The three IMFs are, in fact, the modal responses corresponding to the three dominant modes of vibration of the bridge.

(3) The three acceleration IMFs are integrated in the frequency domain to obtain their respective velocity and displacement time histories. The results show that these three IMFs all satisfy the $\pi/2$ phase difference and $2\pi f$ multiples among the acceleration, velocity, and displacement responses after the frequency domain integration.

(4) The Fast Bayesian FFT method is used to identify the natural frequencies and damping ratios of the bridge from the measured acceleration data. The identified natural frequencies are used to update the design document-based finite element model of the bridge together with the particle swarm optimization algorithm.

(5) Based on the updated model and the measured modal responses, the time histories of the three generalized VIFs are successfully identified according to the theory of structural dynamics.

(6) A polynomial VIF model with all the linear terms, quadratic nonlinear terms, and cubic nonlinear terms is used in this study for the twin-box deck. The nine parameters in the polynomial VIF model are successfully identified using the nonlinear least squares fit (NLSF).

(7) The self-adaptive simplification method (SASM) is used to assess the importance of each term in the polynomial VIF model. It is found that the quadratic nonlinear terms in the polynomial VIF model could be taken away without affecting the accuracy of the VIF model for the concerned bridge. The simplified polynomial VIF model performs well in describing the relationship between the VIF parameters and mean wind speed.

Nevertheless, the VIF model with the parameters identified from the VIV event used in this study should be further examined if it is applicable for a new VIV event whose modes are different from the VIV event used in this study.

Data Availability

The data used to support the findings of this study are available from the corresponding author upon request.

Disclosure

Any opinions and conclusions presented in this paper are entirely those of the authors.

Conflicts of Interest

The authors declare that they have no conflicts of interest.

Authors' Contributions

Shang-Jun Jiang contributed to the conceptualization of the study, methodology, formal analysis, visualization, data curation, software analysis, and writing the original draft. You-Lin Xu contributed to the conceptualization, methodology, investigation, validation, resources, project administration, funding acquisition, supervision, and review and editing of the manuscript. Jin Zhu contributed to the supervision, investigation, and software analysis. Guo-Qing Zhang contributed to the software analysis, investigation, and data curation. Dan-Hui Dan contributed to the investigation and data curation.

Acknowledgments

References

[1] J. Dai, Z. D. Xu, and S. J. Dyke, "Robust control of vortex-induced vibration in flexible bridges using an active tuned mass damper," *Structural Control and Health Monitoring*, vol. 29, no. 8, Article ID e2980, 2022.

[2] J. Zhu, Z. L. Xiong, H. Y. Xiang, X. Huang, and Y. L. Li, "Ride comfort evaluation of stochastic traffic flow crossing long-span suspension bridge experiencing vortex-induced vibration," *Journal of Wind Engineering and Industrial Aerodynamics*, vol. 219, Article ID 104794, 2021.

[3] G. Q. Zhang, B. Wang, Q. Zhu, and Y. L. Xu, "Dynamic behavior and ride comfort of a vehicle moving on a long suspension bridge within multi-mode lock-in regions," *Journal of Wind Engineering and Industrial Aerodynamics*, vol. 234, Article ID 105345, 2023.

[4] T. Kumarasena, R. H. Scanlan, and F. Ehsan, "Wind-induced motions of deer Isle bridge," *Journal of Structural Engineering*, vol. 117, no. 11, pp. 3356–3374, 1991.

[5] A. Larsen, S. Esdahl, J. E. Andersen, and T. Vejrum, "Storebælt suspension bridge – vortex shedding excitation and mitigation by guide vanes," *Journal of Wind Engineering and Industrial Aerodynamics*, vol. 88, no. 2-3, pp. 283–296, 2000.

[6] J. H. Macdonald, P. A. Irwin, and M. S. Fletcher, "Vortex-induced vibrations of the Second Severn Crossing cable-stayed bridge—full-scale and wind tunnel measurements," *Proceedings of the Institution of Civil Engineers-Structures and Buildings*, vol. 152, no. 2, pp. 123–134, 2002.

[7] Y. Hwang, S. Kim, and H. K. Kim, "Cause investigation of high-mode vortex-induced vibration in a long-span suspension bridge," *Structure and Infrastructure Engineering*, vol. 16, no. 1, pp. 84–93, 2020.

[8] H. Li, S. J. Laima, J. P. Ou et al., "Investigation of vortex-induced vibration of a suspension bridge with two separated steel box girders based on field measurements," *Engineering Structures*, vol. 33, no. 6, pp. 1894–1907, 2011.

[9] Y. J. Ge, L. Zhao, and J. X. Cao, "Case study of vortex-induced vibration and mitigation mechanism for a long-span suspension bridge," *Journal of Wind Engineering and Industrial Aerodynamics*, vol. 220, Article ID 104866, 2022.

[10] F. Ehsan and R. H. Scanlan, "Vortex-Induced vibrations of flexible bridges," *Journal of Engineering Mechanics*, vol. 116, no. 6, pp. 1392–1411, 1990.

[11] R. H. Scanlan, "On the state-of-the-art methods for calculation of flutter, vortex-induced and buffeting response of bridge structures," FHWA-RD-80-50 Final Report, Rosap, Washington, DC, USA, 1981.

[12] J. Wu and F. Chang, "Aerodynamic parameters of across-wind self-limiting vibration for square sections after lock-in in smooth flow," *Journal of Sound and Vibration*, vol. 330, no. 17, pp. 4328–4339, 2011.

[13] H. Barhoush, A. H. Namini, and R. A. Skop, "Vortex shedding analysis by finite elements," *Journal of Sound and Vibration*, vol. 184, no. 1, pp. 111–127, 1995.

[14] R. E. D. Bishop and A. Y. Hassan, "The lift and drag forces on a circular cylinder oscillating in a flowing fluid," *Proceedings of the Royal Society of London Series A: Mathematical and Physical Sciences*, vol. 277, no. 1368, pp. 51–75, 1964.

[15] R. T. Hartlen and I. G. Currie, "Lift-oscillator model of vortex-induced vibration," *Journal of the Engineering Mechanics Division*, vol. 96, no. 5, pp. 577–591, 1970.

[16] T. Wu and A. Kareem, "An overview of vortex-induced vibration (VIV) of bridge decks," *Frontiers of Structural and Civil Engineering*, vol. 6, no. 4, pp. 335–347, 2012.

[17] L. D. Zhu, X. L. Meng, and Z. S. Guo, "Nonlinear mathematical model of vortex-induced vertical force on a flat closed-box bridge deck," *Journal of Wind Engineering and Industrial Aerodynamics*, vol. 122, pp. 69–82, 2013.

[18] Q. Zhu, Y. L. Xu, L. D. Zhu, and B. Y. Chen, "A semi-empirical model for vortex-induced vertical forces on a twin-box deck under turbulent wind flow," *Journal of Fluids and Structures*, vol. 71, pp. 183–198, 2017.

[19] L. D. Zhu, X. L. Meng, L. Q. Du, and M. C. Ding, "A simplified nonlinear model of vertical vortex-induced force on box decks for predicting stable amplitudes of vortex-induced vibrations," *Engineering*, vol. 3, no. 6, pp. 854–862, 2017.

[20] Y. L. Xu and Y. Xia, *Structural Health Monitoring of Long-Span Suspension Bridges*, Spon Press, Taylor & Francis, Oxfordshire, UK, 2012.

[21] P. Liu, X. L. Chu, W. Cui, L. Zhao, and Y. J. Ge, "Bayesian inference based parametric identification of vortex-excited force using on-site measured vibration data on a long-span bridge," *Engineering Structures*, vol. 266, Article ID 114597, 2022.

[22] H. Li, S. J. Laima, Q. Q. Zhang, N. Li, and Z. Q. Liu, "Field monitoring and validation of vortex-induced vibrations of a long-span suspension bridge," *Journal of Wind Engineering and Industrial Aerodynamics*, vol. 124, pp. 54–67, 2014.

[23] Q. Zhu, Y. L. Xu, L. D. Zhu, and H. Li, "Vortex-induced vibration analysis of long-span bridges with twin-box decks under non-uniformly distributed turbulent winds," *Journal of Wind Engineering and Industrial Aerodynamics*, vol. 172, pp. 31–41, 2018.

[24] K. Dragomiretskiy and D. Zosso, "Variational mode decomposition," *IEEE Transactions on Signal Processing*, vol. 62, no. 3, pp. 531–544, 2014.

[25] Y. B. Yang, H. Xu, Z. L. Wang, and K. Shi, "Using vehicle-bridge contact spectra and residue to scan bridge's modal properties with vehicle frequencies and road roughness eliminated," *Structural Control and Health Monitoring*, vol. 29, no. 8, Article ID e2968, 2022.

[26] P. H. Ni, J. Li, H. Hao et al., "Time-varying system identification using variational mode decomposition," *Structural Control and Health Monitoring*, vol. 25, no. 6, Article ID e2175, 2018.

[27] H. Zhu, Y. J. Zhou, and Y. M. Hu, "Displacement reconstruction from measured accelerations and accuracy control of integration based on a low-frequency attenuation algorithm," *Soil Dynamics and Earthquake Engineering*, vol. 113, Article ID 106122, 2020.

[28] L. J. Lu, H. F. Zhou, Y. Q. Ni, and F. Dai, "Output-only modal analysis for non-synchronous data using stochastic sub-space identification," *Engineering Structures*, vol. 230, Article ID 111702, 2021.

[29] M. Pedram, A. Esfandiari, and M. R. Khedmati, "Finite element model updating using strain-based power spectral density for damage detection," *Structural Control and Health Monitoring*, vol. 23, no. 11, pp. 1314–1333, 2016.

[30] C. X. Qu, T. H. Yi, and H. N. Li, "Mode identification by eigensystem realization algorithm through virtual frequency response function," *Structural Control and Health Monitoring*, vol. 26, no. 10, Article ID e2429, 2019.

[31] F. L. Zhang, Y. P. Yang, H. B. Xiong, J. H. Yang, and Z. Yu, "Structural health monitoring of a 250-m super-tall building and operational modal analysis using the fast Bayesian FFT method," *Structural Control and Health Monitoring*, vol. 26, Article ID e2383, 2019.

[32] S. Au, "Fast Bayesian ambient modal identification in the frequency domain, Part II: posterior uncertainty," *Mechanical Systems and Signal Processing*, vol. 26, pp. 76–90, 2012.

[33] K. Madsen, H. B. Nielsen, and O. Tingleff, "Methods for nonlinear least squares problems," *Lecture Note*, vol. 38, no. 7, pp. 13–33P, 1999.